arXiv:2405.00292v3 [cond-mat.mes-hall] 4 Sep 2024

Phase shifts, band geometry and responses in triple-Q charge and spin density waves

Ying-Ming Xie[1,*] and Naoto Nagaosa[1,2,†]

[1] *RIKEN Center for Emergent Matter Science (CEMS), Wako, Saitama 351-0198, Japan*
[2] *Fundamental Quantum Science Program, TRIP Headquarters, RIKEN, Wako 351-0198, Japan*

(Dated: September 5, 2024)

Triple-Q density waves are commonly found in various materials, such as charge density waves in transition metal dichalcogenides and spin density waves (skyrmion crystals) in B20 compounds. Compared to single-Q density waves, triple-Q density waves possess an additional internal degree of freedom—a phase shift arising from the phase of the order parameters, in addition to the translations of the density waves. In this study, we systematically investigate the significant effects stemming from both triple-Q CDW and SDW order parameters, with particular emphasis on potential phase shifts. We demonstrate that these phase shifts play a crucial role in influencing the interference effects of triple-Q density waves on electronic states. Due to such interference, the band geometry in the momentum space becomes nontrivial at the hot spots, where multiband Dirac-like fermions are induced near the Fermi energy. Furthermore, we explicitly establish that the nontrivial band geometry, combined with symmetry-breaking induced by phase shifts, leads to a variety of intriguing linear and nonlinear responses.

Introduction— For the incommensurate density waves, there are possible phase degrees of freedom. For example, the incommensurate density waves exhibit an exotic gapless collective excitation — phason. These phasons can be excited with an electric field beyond the threshold, leading to the so-called depinning phenomena. Such phenomena have been observed in both charge density wave (CDW) and spin density wave (SDW) systems [1–7]. Moreover, the CDWs and SDWs often share similar physics with each other. Recently, considerable efforts have been devoted to identifying the common physics shared by various density wave systems [8–10].

Unlike single-Q density waves, triple-Q density waves further exhibit an internal phase shift degree of freedom made from the phase of the order parameters, which determines the structure of triple-Q density waves. The phase shifts are naturally expected to appear in multi-Q incommensurate density waves as well. Especially, the incommensurate triple-Q CDW systems are widely recognized in low-dimensional materials, such as layered transition-metal dichalcogenides (TMDC) 1T TaS_2, 1T $TiSe_2$, 2H $TaSe_2$ [11, 12], while triple-Q SDWs are commonly found in noncolinear magnetic materials, such as skymrion crystals (SkX) [13–16]. Moreover, the important effects of phase shifts on the SkX were recently highlighted [17–19], which play a crucial role in affecting the scalar spin chirality and lowering the rotational symmetry in SkX [18]. However, theoretical work that studies the impacts of the interference of triple-Q density waves with phase shifts on the electronic states in a unified fashion is still lacking.

In this work, we present a minimal theory to capture the phase shifts, band geometry, and their interplay in various linear and nonlinear responses in two-dimensional triple-Q density wave systems. The theoretical framework is applied equally to both triple-Q CDWs and SDWs. We demonstrate that the interference of triple-Q density waves can influence the electronic band geometry at the hot spots, creating multiband Dirac Hamiltonians. Especially, we highlight that phase shifts play a critical role in modifying the geometry of low-energy bands. We also explicitly show that the nontrivial band geometry, along with possible inversion or rotational symmetry breaking induced by phase shifts, enables a rich variety of linear and nonlinear responses in incommensurate triple-Q CDW and SDW systems.

Symmetry classifications of triple-Q density waves— Let us first present the form of triple-Q density waves in two dimensions from the symmetry point of view. Without loss of generality, the three Q vectors are defined as $\boldsymbol{Q}_1 = (1,0)Q, \boldsymbol{Q}_2 = (-\frac{1}{2}, \frac{\sqrt{3}}{2})Q, \boldsymbol{Q}_3 = (-\frac{1}{2}, -\frac{\sqrt{3}}{2})Q$, where the angle with respect to each other are 120 °. The phase shifts along $\boldsymbol{Q}_\nu$ direction are defined as θ_ν. The structure of CDW/SDW is then determined by $\Theta = \frac{1}{\sqrt{3}}(\theta_1+\theta_2+\theta_3)$, while the other two degrees of freedom given by $\theta_X = \frac{1}{\sqrt{6}}(2\theta_1-\theta_2-\theta_3)$, $\theta_Y = \frac{1}{\sqrt{2}}(\theta_2-\theta_3)$. Here, $\theta_{X(Y)}$ represent the phasons, which are typical low-energy elementary excitations in density wave systems upon translational motion [20, 21]. In this work, to preserve C_{3z} symmetry, we would set $\theta_1 = \theta_2 = \theta_3$. But the coupling to the two phasons given by θ_X and θ_Y is an interesting problem for future study. As shown in Table I, we can classify triple-Q density waves using the irreducible representations of the C_3 point group, where the spin Pauli matrices are defined as σ_j, the phase shift is defined as θ, and the position vector is $\boldsymbol{r}$. In the spinless case, the C_{3z} invariant triple-Q density wave order parameter, i.e., CDW order parameter, is

$$\Delta_{\mathrm{CDW}}(\boldsymbol{r}) = 2\Delta f_A(\boldsymbol{r}) = 2\Delta \sum_{\nu=1}^{3} \cos(\boldsymbol{Q}_\nu \cdot \boldsymbol{r} + \theta_\nu). \quad (1)$$

where Δ denotes the CDW potential, and $f_A(\boldsymbol{r})$ is the basis function of A irreducible representation of C_3 point

* yingming.xie@riken.jp
† nagaosa@riken.jp

TABLE I. Classifications of triple-Q density waves using the irreducible representations of the C_{3z} point group. Here, $\omega = e^{i2\pi/3}$, $\boldsymbol{Q}_1 = (1,0)Q, \boldsymbol{Q}_2 = (-\frac{1}{2}, \frac{\sqrt{3}}{2})Q, \boldsymbol{Q}_3 = (-\frac{1}{2}, -\frac{\sqrt{3}}{2})Q$, σ_j are spin Pauli matrices.

C_3	basis functions	spin matrices
1	$f_A(\boldsymbol{r}) = \sum_{\nu=1}^{3} \cos(\boldsymbol{Q}_\nu \cdot \boldsymbol{r} + \theta)$	σ_0, σ_z
ω	$f_{E_1}(\boldsymbol{r}) = \sum_{\nu=1}^{3} \omega^{\nu-1} \sin(\boldsymbol{Q}_\nu \cdot \boldsymbol{r} + \theta)$	$\sigma_+ = \sigma_x + i\sigma_y$
ω^*	$f_{E_2}(\boldsymbol{r}) = \sum_{\nu=1}^{3} \omega^{1-\nu} \sin(\boldsymbol{Q}_\nu \cdot \boldsymbol{r} + \theta)$	$\sigma_- = \sigma_x - i\sigma_y$

group. In the spinful case, the C_{3z} invariant triple-Q density wave order parameter, i.e., SDW order parameter, is obtained as

$$\Delta_{\mathrm{SDW}}(\boldsymbol{r}) = \frac{\Delta}{2}[f_{E_1}(\boldsymbol{r})\sigma_- + f_{E_2}(\boldsymbol{r})\sigma_+] - \Delta f_A(\boldsymbol{r})\sigma_z. \quad (2)$$

Here, $f_{E_1}(\boldsymbol{r})$ and $f_{E_2}(\boldsymbol{r})$ (see Table I) are the basis functions of E_1 and E_2 irreducible representations of C_3 group. We can rewrite the form of $\Delta_{\mathrm{SDW}}(\boldsymbol{r})$ as

$$\Delta_{\mathrm{SDW}}(\boldsymbol{r}) = \sum_i \boldsymbol{S}_i^{\mathrm{spiral}} \cdot \boldsymbol{\sigma}, \quad (3)$$

and obtain the triple-Q spiral spin textures [18]

$$\boldsymbol{S}_i^{\mathrm{spiral}} = \Delta \sum_{\nu=1}^{3} (\sin \mathcal{Q}_\nu \cos\phi_\nu, \sin \mathcal{Q}_\nu \sin\phi_\nu, -\cos \mathcal{Q}_\nu) \quad (4)$$

with $\mathcal{Q}_\nu = \boldsymbol{Q}_\nu \cdot \boldsymbol{r}_i + \theta_\nu$, $\phi_\nu = \frac{2\pi}{3}(\nu - 1)$. Here, $\boldsymbol{Q}_\nu$ is the wave vector of ν-th spiral, and $\theta_\nu = \theta$. For the sake of simplicity, we neglect the spin-orbit interaction in our model so that the direction of the spin-rotating plane does not matter. We shall also focus on the simplest case that the order parameter only exhibits the spatial and spin degree of freedom.

Real space landscape and topology of triple-Q density waves— To visualize these order parameters and highlight the effects of the phase shift θ on the triple-Q density waves, we plot the real space landscape of triple-Q CDW and triple-Q SDW with various θ in Fig. 1.

Figs. 1(a) and (b) display the CDW order parameter $\Delta_{\mathrm{CDW}}(\boldsymbol{r})$ at $\theta = 0$ and $\theta = \pi/6$. Interestingly, it can be seen that the presence of finite θ can break the inversion symmetry. To show the real space feature of SDW order $\Delta_{\mathrm{SDW}}(\boldsymbol{r})$, the spiral spin textures given by $\boldsymbol{S}^{\mathrm{spiral}}$ at $\theta = 0$ is plotted in Fig. 1(c), which displays as a skyrmion crystal. Then we study the topology of the spiral spin textures more explicitly. The calculated skyrmion charge $N_{sk} = \frac{1}{4\pi}\int\int d^2\boldsymbol{r}\boldsymbol{s}\cdot(\partial_x\boldsymbol{s}\times\partial_y\boldsymbol{s})$ as a function of the phase shift θ with $\boldsymbol{s}$ being the unit vector of spin normalized from $\boldsymbol{S}$ is shown in Fig. 1(d). Interestingly, we find that the skyrmion charge N_{sk} is quantized at ± 1 except for flipping sign at $\theta = \frac{(2n+1)\pi}{6}$ (n are integers). At these angles where N_{sk} changes sign, it can be seen that the spiral spin textures $\boldsymbol{S}^{\mathrm{spiral}}$ would display as a meron-antimeron crystal [Fig. 1(e)]. The spin chirality of meron and antimeron is opposite and would cancel with each other

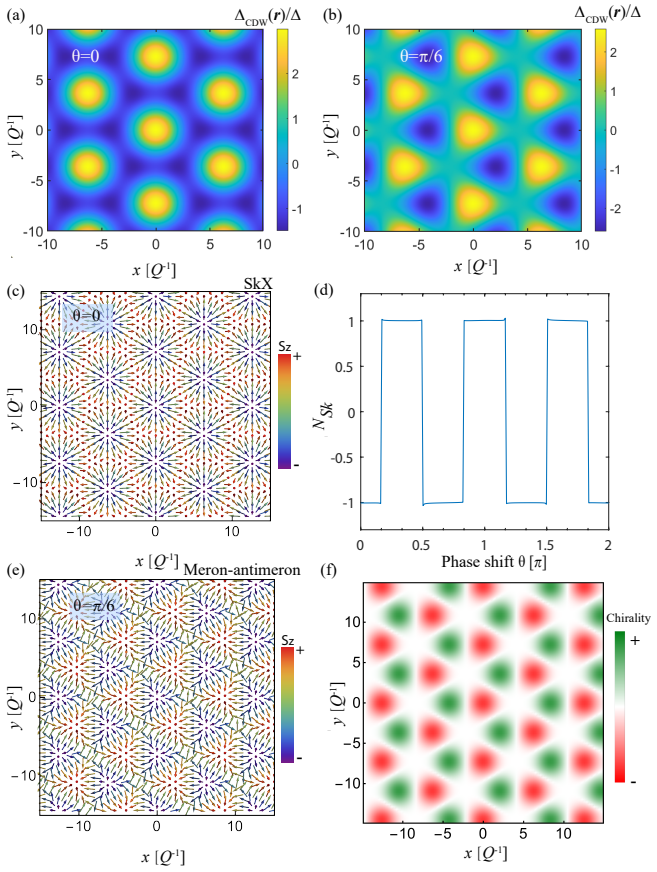


FIG. 1. (a) and (b) The real-space dependence of triple-Q CDW potential $\Delta_{\mathrm{CDW}}(\boldsymbol{r})$ at $\theta = 0$ and $\theta = \pi/6$, respectively. (c) and (e) The triple-Q spiral spin textures at $\theta = 0$ and $\theta = \frac{\pi}{6}$, respectively. (d) The total skyrmion charge N_{sk} of each unit cell versus the phase shift θ calculated from the normalized spin vectors $\boldsymbol{s}$. (f) The real-space spin chirality $\chi = \boldsymbol{S}_i \cdot (\boldsymbol{S}_j \times \boldsymbol{S}_k)$, where the site indcies i, j, k are in counterclockwise order.

[Fig. 1(f)]. In the SkX systems, it is known that the SkX can be tuned into the meron-antimeron crystal via external magnetic fields [17, 22]. But the phase shift θ generally is hard to be continuously tuned in experiments. In practice, the phase shift θ in our model can be estimated by mimicking triple-Q CDW and SDW real space patterns in a given experiment.

Dirac Hamiltonians induced by triple-Q density waves— Beyond the real-space topology, next we show that the triple-Q density wave order parameters can alter the geometry properties of Bloch bands using a weak-coupling approach. Specifically, we point out that the triple-Q density waves can spontaneously induce Dirac-like physics near the Fermi energy. As the focus of this work is the triple-Q order parameter, we shall set the band dispersion to be the simplest one: $\xi_{\boldsymbol{p}} = \frac{\boldsymbol{p}^2}{2m} - \mu$, where m is an effective mass, μ is the chemical potential. In practice, the chemical potential μ should be located near the Fermi energy where the CDW nesting happens.

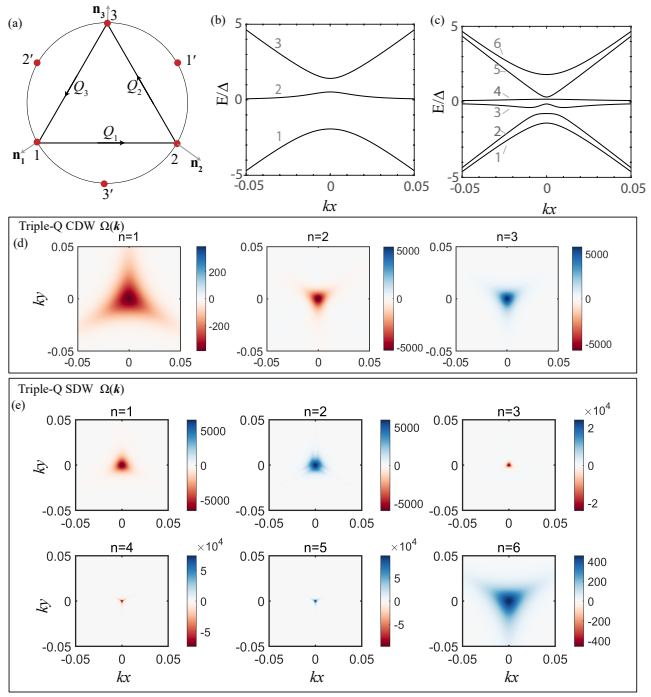


FIG. 2. (a) Illustration of the six 'hot spots' (red dots) on the Fermi circle, which are connected through the triple-Q vectors. Note that the dispersion of electrons is given by $\xi_{\boldsymbol{p}} = \frac{p^2}{2m} - \mu$, and $\hat{n}_i$ is simply the unit vector for the direction of the hot-spot momentum $\boldsymbol{p}_i$, where the two density wave order parameters interfere. (b) and (c) respectively, show the band structures of triple-Q CDW and triple-Q SDW along $(k_x, 0)$ direction given by the effective Hamiltonians, where the phase shift is set to be $\theta = \pi/4$. (d) and (f) show the Berry curvature $\Omega(\boldsymbol{k})$ (in units of a^2 and a is the lattice constant) of each band in (b) and (c), respectively. We set $v_F = 100, \Delta = 1$ in calculations. Note that (d) and (e) only show the distribution near one set of hot spots.

As shown in Fig. 2(a), there are six 'hot spots' (labeled as red dots) that the triple-Q order parameter would couple near Fermi energy. These hot spots can be classified into two sets, i.e., 1,2,3 and 1′,2′,3′. The single-particle dispersion near the hot spots can be approximated as

$$\epsilon_{\boldsymbol{k}} = v_F \hat{\boldsymbol{n}}_i \cdot \boldsymbol{k}, \tag{5}$$

where v_F is the Fermi velocity, and unit vectors $\hat{\boldsymbol{n}}_1 = (-\frac{\sqrt{3}}{2}, -\frac{1}{2}), \hat{\boldsymbol{n}}_2 = (\frac{\sqrt{3}}{2}, -\frac{1}{2}), \hat{\boldsymbol{n}}_3 = (0, 1)$, and the momentum $\boldsymbol{k}$ is measured with respect to the hot-spot momentum $\boldsymbol{p}_i$ with $\boldsymbol{k} = \boldsymbol{p} - \boldsymbol{p}_i$.

Next, we present the low-energy effective Hamiltonians with the triple-Q order parameter, which would induce the coupling between these hot spots, i.e., band folding. Here, we assume the coupling is weak enough so that these hot spots do not overlap with each other. As we will soon see, the additional phase shift θ modifies the low-energy band dispersions.

We first focus on the triple-Q CDW. The effective Hamiltonian of the CDW state can be written as $\mathcal{H} = \sum \Phi_{\boldsymbol{k}}^\dagger H_{\rm CDW}(\boldsymbol{k}) \Phi_{\boldsymbol{k}}$ with $\Phi_{\boldsymbol{k}} = (c_{1\boldsymbol{k}}, c_{2\boldsymbol{k}}, c_{3\boldsymbol{k}})^T$ and

$$H_{\rm CDW}(\boldsymbol{k}) = \begin{pmatrix} v_F \boldsymbol{k}\cdot\hat{\boldsymbol{n}}_1 & \Delta e^{-i\theta} & \Delta e^{i\theta} \\ \Delta e^{i\theta} & v_F \boldsymbol{k}\cdot\hat{\boldsymbol{n}}_2 & \Delta e^{-i\theta} \\ \Delta e^{-i\theta} & \Delta e^{i\theta} & v_F \boldsymbol{k}\cdot\hat{\boldsymbol{n}}_3 \end{pmatrix}, \tag{6}$$

where $\boldsymbol{k}$ is measured with respect to the hot spots. Note that $\boldsymbol{k} = 0$ is the Gamma point of the folded Brillouin zone. The effective Hamiltonian $H'_{\rm CDW}(\boldsymbol{k})$ defined in the other group $(c_{1'\boldsymbol{k}}, c_{2'\boldsymbol{k}}, c_{3'\boldsymbol{k}})^T$ can be obtained by replacing $\hat{\boldsymbol{n}}_i$ and θ in $H_{\rm CDW}(\boldsymbol{k})$ with $\hat{\boldsymbol{n}'}_i = -\hat{\boldsymbol{n}}_i$ and $-\theta$.

To emphasize the nontrivial band geometry encoded in the effective Hamiltonian, we show that $H_{\rm CDW}(\boldsymbol{k})$ can be actually mapped to a three-band Dirac Hamiltonian. Note that the multi-band Dirac Hamiltonian in this work is defined as all non-vanishing terms in the Hamiltonian are linearly proportional to k_+ or k_-[23]. As shown in Supplementary Material (SM) [24], the eigenstates of $H_{\rm CDW}(\boldsymbol{k})$ at $\boldsymbol{k} = 0$ can be labeled with the eigenvalue of C_{3z} operation: $C_{3z}\left|E_{J,m}\right\rangle = e^{-i\frac{2m\pi}{3}}\left|E_{J,m}\right\rangle$, where the total angular momentum $J = 1$, the magnetic angular momentum $m = 0, \pm 1$. After projecting the $H_{\rm CDW}(\boldsymbol{k})$ into the 'good' basis spanned by $(\left|E_{1,0}\right\rangle, \left|E_{1,-1}\right\rangle, \left|E_{1,1}\right\rangle)$, the effective Hamiltonian is represented as a three-band Dirac Hamiltonian:

$$H^{\rm eff}_{\rm CDW}(\boldsymbol{k}) = \begin{pmatrix} E_{1,0} & -\frac{i}{2}v_F k_- & -\frac{i}{2}v_F k_+ \\ \frac{i}{2}v_F k_+ & E_{1,-1} & -\frac{i}{2}v_F k_- \\ \frac{i}{2}v_F k_- & \frac{i}{2}v_F k_+ & E_{1,1} \end{pmatrix} \tag{7}$$

where $k_\pm = k_x \pm i k_y$, $E_{J,m} = 2\Delta\cos(\theta - \frac{2m\pi}{3})$. Importantly, the phase shift plays a significant role in affecting the Dirac mass. It is also noted that the multi-band Dirac Hamiltonian can also be induced in double-Q when more than two hot spots are folded together simultaneously (see SM [24] for details). We shall focus on the triple-Q density waves case below as the phase shift degrees of freedom in single-Q and double-Q ones are absent.

Similar physics can also be induced by the triple-Q SDW order parameters. Specifically, we can first obtain the effective Hamiltonian near the first set of hot spots (1,2, and 3) as

$$H_{\rm SDW}(\boldsymbol{k}) = \begin{pmatrix} v_F \boldsymbol{k}\cdot\hat{\boldsymbol{n}}_1 & \Delta \boldsymbol{S}_{-\boldsymbol{Q}_1}\cdot\boldsymbol{\sigma} & \Delta \boldsymbol{S}_{\boldsymbol{Q}_3}\cdot\boldsymbol{\sigma} \\ \Delta \boldsymbol{S}_{\boldsymbol{Q}_1}\cdot\boldsymbol{\sigma} & v_F \boldsymbol{k}\cdot\hat{\boldsymbol{n}}_2 & \Delta \boldsymbol{S}_{-\boldsymbol{Q}_2}\cdot\boldsymbol{\sigma} \\ \Delta \boldsymbol{S}_{-\boldsymbol{Q}_3}\cdot\boldsymbol{\sigma} & \Delta \boldsymbol{S}_{\boldsymbol{Q}_2}\cdot\boldsymbol{\sigma} & v_F \boldsymbol{k}\cdot\hat{\boldsymbol{n}}_3 \end{pmatrix}, \tag{8}$$

where the basis is $(c_{1\boldsymbol{k}}, c_{2\boldsymbol{k}}, c_{3\boldsymbol{k}})^T \otimes (\uparrow, \downarrow)^T$, and $\boldsymbol{S}_{\pm\boldsymbol{Q}_\nu} = (\mp\frac{i}{2}\cos\phi_\nu, \mp\frac{i}{2}\sin\phi_\nu, \mp\frac{1}{2})e^{i\pm\theta}$. By replacing $\boldsymbol{S}_{\pm\boldsymbol{Q}_\nu}$ with $\boldsymbol{S}_{\mp\boldsymbol{Q}_\nu}$ and $\hat{\boldsymbol{n}}_i$ with $\hat{\boldsymbol{n}}'_i$, the low-energy Hamiltonian $H'_{\rm SDW}(\boldsymbol{k})$ near the other set of hot spots (1′, 2′, 3′) can be obtained. Also, performing a unitary transform and rewriting the Hamiltonian in the basis $\left|E\right\rangle_{J,m} \otimes \{\uparrow, \downarrow\}$, a six-band effective Hamiltonian can be obtained (see SM Note 1 for the detailed form).

One important property of the Dirac Hamiltonian is to enable the Berry curvature, which has been associated with various topological materials. Here, we show

TABLE II. Possible responses induced triple-Q density wave order parameters from symmetry principle. Here, AHE, SHG, MOE, VHE label the anomalous Hall effect, second harmonic generation, magnetoptical effect, valley Hall effect.

Triple-Q	θ	key symmetries	responses
CDW	$\theta = \frac{n\pi}{3}$	T, I, C_{3z}, M_x, M_y	
	$\theta \neq \frac{n\pi}{3}$	T,~~I~~, C_{3z}, ~~M_x~~, M_y	SHG, VHE
SDW	$\theta = \frac{n\pi}{3}$	~~T~~,~~I~~, C_{2z}, C_{3z}	AHE, MOE
	$\theta \neq \frac{n\pi}{3}$	~~T~~,~~I~~, ~~C_{2z}~~, C_{3z}	AHE, MOE SHG

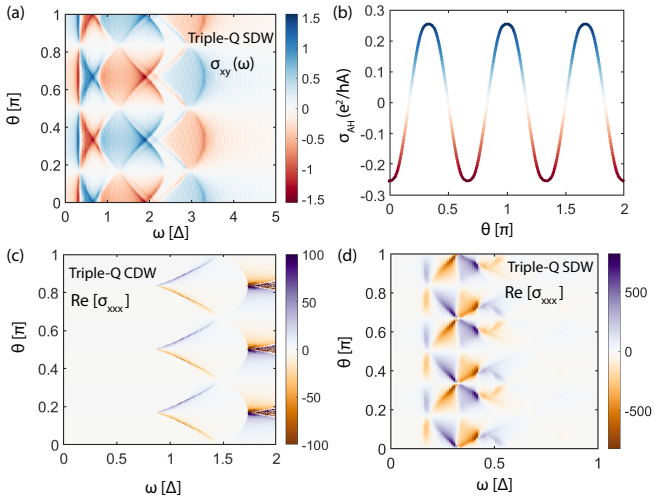


FIG. 3. (a) The magnetoptical conductivity $\sigma_{xy}(\omega)$ as a function of the phase shift θ and the photon frequency ω, where the colorbar is in unit of $\frac{e^2}{h}$. (b) The anomalous Hall conductivity as a function of photon frequency. (c) and (d), respectively, show the real part of the second-harmonic response tensor $\mathrm{Re}[\sigma_{xxx}(2\omega;\omega,\omega)]$, which is in units of $e^3/(2\hbar^2)$. The chemical potential in this figure is fixed at the position of hot spots, and the temperature is zero temperature limit with $T = 0.01\Delta$.

that the triple-Q density wave order parameters can induce Berry curvature on the simplest quadratic band. The band structures given by $H_{\mathrm{CDW}}(\boldsymbol{k})$ and $H_{\mathrm{SDW}}(\boldsymbol{k})$ are shown Figs. 2(b) and 2(c), respectively. The Berry curvature of these bands can be easily calculated, as shown in Fig. 2(d) for the triple-Q CDW and Fig. 2(e) for the triple-Q SDW. Moreover, we find that the phase shift would affect the Berry curvature significantly. For example, the Berry curvature vanishes at $\theta = \frac{n\pi}{3}$ and $\theta = \frac{(2n+1)\pi}{6}$ for the $H_{\mathrm{CDW}}(\boldsymbol{k})$ and $H_{\mathrm{SDW}}(\boldsymbol{k})$ respectively, while the latter exactly corresponds to the presence of meron-antimron crystals in real space.

Linear and nonlinear responses in triple-Q density wave systems— Due to the presence of nontrivial band geometry, we expect that triple-Q density wave order parameters would naturally result in some interesting linear and nonlinear responses. Let us identify the symmetries dedicated by the triple-Q density wave order parameter first. Either from the real-space landscape or the effective Hamiltonian (see SM [24] for detailed symmetry analysis), we can identify that the triple-Q CDW order parameter $\Delta_{\mathrm{CDW}}(\boldsymbol{r})$ preserves time-reversal symmetry at generic θ but breaks inversion only when $\theta \neq \frac{n\pi}{3}$. Consequently, a second harmonic generation (SHG) solely induced by the triple-Q CDW would be expected. Furthermore, if we consider the two sets of hotspots within CDWs as distinct valleys within momentum space, the Berry curvature contrasts between these valleys due to time-reversal symmetry. This contrast can induce valley Hall effects [25–28].

On the other hand, it can be shown that the triple-Q SDW order parameter $\Delta_{\mathrm{SDW}}(\boldsymbol{r})$ would break both time-reversal and inversion symmetry regardless of the value of θ, which stems from the presence of spiral spin textures. The broken time-reversal symmetry allows the anomalous Hall effect (AHE) and magnetoptical responses, while the further broken inversion symmetry is crucial for the nonreciprocal or nonlinear responses [29]. The resulting key point group symmetry generators induced by the $\Delta_{\mathrm{SDW}}(\boldsymbol{r})$ are C_{2z} at $\theta = \frac{n\pi}{3}$, and C_{2z} would be broken when $\theta \neq \frac{n\pi}{3}$. Note that, unlike triple-Q CDWs, the point group formed by the unitary operations of triple-Q SDWs is chiral, where all mirror symmetries are broken. As a result, the nonreciprocal nonlinear responses can be supported in triple-Q SDW systems as well. To be clear, the above discussions are explicitly summarized in Table II. Note that as imposed by us, the C_{3z} symmetry is also preserved at generic θ for triple-Q density waves in this work. When the C_{3z} symmetry is absent, such as broken by the external strain, other interesting effects may further be allowed (see SM Note 3 for a discussion of nonlinear Hall effects [30–32] in strained SDW states).

To be more explicit, we now calculate some representative linear and nonlinear responses from the effective triple-Q CDW and SDW Hamiltonians. The representative linear responses: AHE and magnetoptical conductivity can be obtained from the Kubo formula [33]. Using the triple-Q effective Hamiltonian $H_{\mathrm{SDW}}(\boldsymbol{k})$ and $H'_{\mathrm{SDW}}(\boldsymbol{k})$ (these two contributions need to be summed up), the calculated magnetoptical conductivity $\sigma_{xy}(\omega)$ as a function the frequency ω and the phase shift θ, and the calculated AHE conductivity σ_{AH} versus θ are shown in Fig. 3 (a) and (b), respectively. The finite AHE and magnetoptical effect are expected due to the nontrivial band geometry near Fermi energy. It is worth noting that the AHE vanishes at $\theta = \frac{(2n+1)\pi}{6}$, while remaining finite at other phase shifts. Such observation is consistent with the real-space topology discussed in Fig. 1: the meron-antimeron crystal appears at $\theta = \frac{(2n+1)\pi}{6}$, while the skyrmion crystals that possess topological Hall effects would appear at other phase shifts.

Finally, we highlight the representative nonlinear responses enabled by the triple-Q density wave order parameters. Nonlinear responses have been a subject of intense study in recent years (see reviews [29, 34, 35] for experimental and theoretical details). Observing

these nonlinear responses requires certain symmetry conditions. For instance, SHG necessitates inversion symmetry breaking, while magnetochiral anisotropy requires the breaking of both inversion and time-reversal symmetry. Additionally, band geometry plays a significant role in enhancing nonlinear responses as well [34, 36]. Guided by these principles, we anticipate that a triple-Q density wave state could be highly effective in exploring nonlinear responses due to its involvement in both symmetry breaking and nontrivial band geometry. As a demonstration, the second harmonic generation response tensor $\sigma_{xxx}(2\omega;\omega,\omega)$ calculated from the effective Hamiltonians of triple-Q CDW and SDW are shown in Fig. 3(c) to (d) (see the explicit SHG formalism in refs. [37, 38] or in Supplementary Note 2). Remarkably, the SHG is finite at a wide parameter region. Some special phase shifts where the SHG vanishes also match with the expectations: (i) $\theta = \frac{2n\pi}{3}$ for triple-Q CDW due to the restoration of inversion symmetry, (ii) $\theta = \frac{n\pi}{3}$ and $\theta = \frac{(2n+1)\pi}{6}$ for triple-Q CDW and SDW, where the inversion symmetry is still broken but the Berry curvature vanishes. Additionally, as presented in Supplementary Information Note 1, we also can show that the magnetochiral anisotropy would be supported in tripe-Q SDW at $\theta \neq \frac{n\pi}{3}$ with C_{2z} symmetry broken.

Discussion— It is noteworthy that various intriguing linear and nonlinear responses have been experimentally studied in several triple-Q density wave systems. For example, it was observed that the inversion and mirror symmetry are broken in the triple-Q CDW system 1T $TiSe_2$ [39], which are indeed consistent with our analysis in Table II of triple-Q CDW with finite phase shifts $\theta \neq \frac{n\pi}{3}$. On the other hand, it was suggested that there are both SkX (called A phase) and meron-antimeron crystal (called IC-1 phase) in Gd_2PdSi_3[17]. In ref. [40], the magnetoptical Kerr effect (MOKE) was experimentally studied in Gd_2PdSi_3. Indeed, the SkX region displays much more salient MOKE than the meron-antimeron crystal, which is also aligned with our analysis in Fig. 3(a). Additionally, the chiral transport effect was observed in Kagome triple-Q CDW metal CsV_3Sb_5 and indicates time-reversal symmetry breaking [41]. To capture such features, we believe that the multi-sublattice degree of freedom in CsV_3Sb_5 plays an important role and results in complex triple-Q order parameters. How the phase shift plays a role in affecting the complex triple-Q CDW order parameters remains an interesting future problem.

It is interesting to note that for the triple-Q CDW, the inversion can only be broken with a non-vanishing phase shift (see Table II). Motivated by this observation, we propose to measure the SHG in the triple-Q CDW, where the parent crystal structure is centrosymmetric but the triple-Q CDW spontaneously breaks the inversion. In this case, the SHG signal arises from the inversion symmetry breaking of triple-Q CDW, which is directly associated with the presence of phase shifts. Although a related experiment has been conducted in 1T TiSe2 [39], the role of phase shift has not yet been emphasized. Moreover, the observation of other responses listed in Table II, such as the valley Hall effects, would further verify our theory.

Acknowledgements—We are grateful to Hiroki Isobe and Wataru Koshibae for enlightening discussions. N.N. was supported by JSPS KAKENHI Grant No. 24H00197 and 24H02231. N.N. was also supported by the RIKEN TRIP initiative. Y.M.X. acknowledges financial support from the RIKEN Special Postdoctoral Researcher(SPDR) Program.

[1] P. Lee, T. Rice, and P. Anderson, Solid State Communications **14**, 703 (1974).
[2] H. Fukuyama and P. A. Lee, Phys. Rev. B **17**, 535 (1978).
[3] P. A. Lee and T. M. Rice, Phys. Rev. B **19**, 3970 (1979).
[4] L. Sneddon, M. C. Cross, and D. S. Fisher, Phys. Rev. Lett. **49**, 292 (1982).
[5] G. Grüner, Rev. Mod. Phys. **60**, 1129 (1988).
[6] G. Grüner, Rev. Mod. Phys. **66**, 1 (1994).
[7] C. Reichhardt, C. J. O. Reichhardt, and M. V. Milošević, Rev. Mod. Phys. **94**, 035005 (2022).
[8] Y.-M. Xie, Y. Liu, and N. Nagaosa, Phys. Rev. Lett. **133**, 096702 (2024).
[9] Y.-M. Xie, H. Isobe, and N. Nagaosa, arXiv e-prints , arXiv:2404.04789 (2024), arXiv:2404.04789.
[10] M. T. Birch, I. Belopolski, Y. Fujishiro, M. Kawamura, A. Kikkawa, Y. Taguchi, M. Hirschberger, N. Nagaosa, and Y. Tokura, arXiv e-prints , arXiv:2406.01847 (2024), to appear in Nature.
[11] W. L. McMillan, Phys. Rev. B **14**, 1496 (1976).
[12] K. Rossnagel, Journal of Physics: Condensed Matter **23**, 213001 (2011).
[13] S. Mühlbauer, B. Binz, F. Jonietz, C. Pfleiderer, A. Rosch, A. Neubauer, R. Georgii, and P. Böni, Science **323**, 915 (2009).
[14] X. Z. Yu, Y. Onose, N. Kanazawa, J. H. Park, J. H. Han, Y. Matsui, N. Nagaosa, and Y. Tokura, Nature **465**, 901 (2010).
[15] N. Nagaosa and Y. Tokura, Nature Nanotechnology **8**, 899 (2013).
[16] Y. Tokura and N. Kanazawa, Chemical Reviews **121**, 2857 (2021).
[17] T. Kurumaji, T. Nakajima, M. Hirschberger, A. Kikkawa, Y. Yamasaki, H. Sagayama, H. Nakao, Y. Taguchi, T. hisa Arima, and Y. Tokura, Science **365**, 914 (2019).
[18] S. Hayami, T. Okubo, and Y. Motome, Nature Communications **12**, 6927 (2021).
[19] K. Shimizu, S. Okumura, Y. Kato, and Y. Motome, Phys. Rev. B **105**, 224405 (2022).
[20] S. Hoshino and N. Nagaosa, Phys. Rev. B **97**, 024413

(2018).
[21] G. Tatara and H. Fukuyama, Journal of the Physical Society of Japan **83**, 104711 (2014).
[22] X. Z. Yu, W. Koshibae, Y. Tokunaga, K. Shibata, Y. Taguchi, N. Nagaosa, and Y. Tokura, Nature **564**, 95 (2018).
[23] Y.-M. Xie, C.-P. Zhang, J.-X. Hu, K. F. Mak, and K. T. Law, Phys. Rev. Lett. **128**, 026402 (2022).
[24] See Supplementary Material for details, which include: (i) Effective Hamiltonian and symmetry analysis for Triple-Q CDW state; (ii) single-Q and double-Q states; (iii) nonreciprocal transports in triple-Q SDWs; (iv) second harmonic generation responses formalism.
[25] M. Sui, G. Chen, L. Ma, W.-Y. Shan, D. Tian, K. Watanabe, T. Taniguchi, X. Jin, W. Yao, D. Xiao, and Y. Zhang, Nature Physics **11**, 1027 (2015).
[26] Y. Shimazaki, M. Yamamoto, I. V. Borzenets, K. Watanabe, T. Taniguchi, and S. Tarucha, Nature Physics **11**, 1032 (2015).
[27] W. Yao, D. Xiao, and Q. Niu, Phys. Rev. B **77**, 235406 (2008).
[28] J. Yin, C. Tan, D. Barcons-Ruiz, I. Torre, K. Watanabe, T. Taniguchi, J. C. W. Song, J. Hone, and F. H. L. Koppens, Science **375**, 1398 (2022).
[29] Y. Tokura and N. Nagaosa, Nature Communications **9**, 3740 (2018).
[30] I. Sodemann and L. Fu, Phys. Rev. Lett. **115**, 216806 (2015).
[31] Z. Z. Du, H.-Z. Lu, and X. C. Xie, Nature Reviews Physics **3**, 744 (2021).
[32] Q. Ma, S.-Y. Xu, H. Shen, D. MacNeill, V. Fatemi, T.-R. Chang, A. M. Mier Valdivia, S. Wu, Z. Du, C.-H. Hsu, S. Fang, Q. D. Gibson, K. Watanabe, T. Taniguchi, R. J. Cava, E. Kaxiras, H.-Z. Lu, H. Lin, L. Fu, N. Gedik, and P. Jarillo-Herrero, Nature **565**, 337 (2019).
[33] W. Feng, J.-P. Hanke, X. Zhou, G.-Y. Guo, S. Blügel, Y. Mokrousov, and Y. Yao, Nature Communications **11**, 118 (2020).
[34] T. Morimoto, S. Kitamura, and N. Nagaosa, Journal of the Physical Society of Japan **92**, 072001 (2023), https://doi.org/10.7566/JPSJ.92.072001.
[35] N. Nagaosa and Y. Yanase, Annual Review of Condensed Matter Physics **15**, 63 (2024).
[36] T. Morimoto and N. Nagaosa, Science Advances **2**, e1501524 (2016).
[37] D. E. Parker, T. Morimoto, J. Orenstein, and J. E. Moore, Phys. Rev. B **99**, 045121 (2019).
[38] K. Takasan, T. Morimoto, J. Orenstein, and J. E. Moore, Phys. Rev. B **104**, L161202 (2021).
[39] B. T. Fichera, A. Kogar, L. Ye, B. Gökce, A. Zong, J. G. Checkelsky, and N. Gedik, Phys. Rev. B **101**, 241106 (2020).
[40] Y. D. Kato, Y. Okamura, M. Hirschberger, Y. Tokura, and Y. Takahashi, Nature Communications **14**, 5416 (2023).
[41] C. Guo, C. Putzke, S. Konyzheva, X. Huang, M. Gutierrez-Amigo, I. Errea, D. Chen, M. G. Vergniory, C. Felser, M. H. Fischer, T. Neupert, and P. J. W. Moll, Nature **611**, 461 (2022).
[42] T. Yokouchi, N. Kanazawa, A. Kikkawa, D. Morikawa, K. Shibata, T. Arima, Y. Taguchi, F. Kagawa, and Y. Tokura, Nature Communications **8**, 866 (2017).
[43] D. Kaplan, T. Holder, and B. Yan, SciPost Phys. **14**, 082 (2023).
[44] D. Kaplan, T. Holder, and B. Yan, Phys. Rev. Lett. **132**, 026301 (2024).

Supplementary Material for "Phase shifts, band geometry and responses in triple-Q charge and spin density waves"

Ying-Ming Xie [1] and Naoto Nagaosa[1,2]

[1] *RIKEN Center for Emergent Matter Science (CEMS), Wako, Saitama 351-0198, Japan*

[2] *Fundamental Quantum Science Program, TRIP Headquarters, RIKEN, Wako 351-0198, Japan*

Supplementary Note 1. EFFECTIVE HAMILTONIAN AND SYMMETRY ANALYSIS FOR TRIPLE-Q CDW STATE

A. Effective Hamiltonian and symmetry analysis for the Triple-Q CDW state.

As shown in Supplementary Fig. 1 (a) and (b), there are six hot spots connected by the triple-Q vectors. These hot spots can be classified into two groups, i.e., 1,2,3 and 1′,2′,3′. The dispersion $\xi_{\boldsymbol{k}} = \frac{\hbar^2\boldsymbol{k}^2}{2m} - \mu$ near the hot spots can be approximated as

$$\xi_{\boldsymbol{k}} = v_F \hat{\boldsymbol{n}}_i \cdot \boldsymbol{k}, \tag{S1}$$

where v_F is the Fermi velocity, and

$$\hat{\boldsymbol{n}}_1 = (-\frac{\sqrt{3}}{2}, -\frac{1}{2}), \hat{\boldsymbol{n}}_2 = (\frac{\sqrt{3}}{2}, -\frac{1}{2}), \hat{\boldsymbol{n}}_3 = (0, 1). \tag{S2}$$

In real space, the CDW order parameters can be written as

$$\Delta(\boldsymbol{r}_i) = 2\Delta \sum_{\nu} \cos(\boldsymbol{Q}_\nu \cdot \boldsymbol{r}_i + \theta_\nu). \tag{S3}$$

Here,

$$\boldsymbol{Q}_1 = (Q, 0), \boldsymbol{Q}_2 = (-Q/2, \sqrt{3}Q/2), \boldsymbol{Q}_3 = (-Q/2, -\sqrt{3}Q/2). \tag{S4}$$

The effective Hamiltonian of the CDW state can be written as $\mathcal{H} = \sum \Phi^\dagger_{\boldsymbol{k}} H_{\rm CDW}(\boldsymbol{k}) \Phi_{\boldsymbol{k}}$ with $\Phi_{\boldsymbol{k}} = (c_{1\boldsymbol{k}}, c_{2\boldsymbol{k}}, c_{3\boldsymbol{k}})^T$ and

$$H_{\rm CDW}(\boldsymbol{k}) = \begin{pmatrix} v_F\boldsymbol{k}\cdot\hat{\boldsymbol{n}}_1 & \Delta e^{-i\theta_1} & \Delta e^{i\theta_3} \\ \Delta e^{i\theta_1} & v_F\boldsymbol{k}\cdot\hat{\boldsymbol{n}}_2 & \Delta e^{-i\theta_2} \\ \Delta e^{-i\theta_3} & \Delta e^{i\theta_2} & v_F\boldsymbol{k}\cdot\hat{\boldsymbol{n}}_3 \end{pmatrix}, \tag{S5}$$

where $\boldsymbol{k}$ is measured respected from $\boldsymbol{p}_i$ the unit vectors in triple-Q case are $\hat{\boldsymbol{n}}_1 = (-\frac{\sqrt{3}}{2}, -\frac{1}{2}), \hat{\boldsymbol{n}}_2 = (\frac{\sqrt{3}}{2}, -\frac{1}{2}), \hat{\boldsymbol{n}}_3 = (0, 1)$. Near the other group hot spots, the effective Hamiltonian becomes

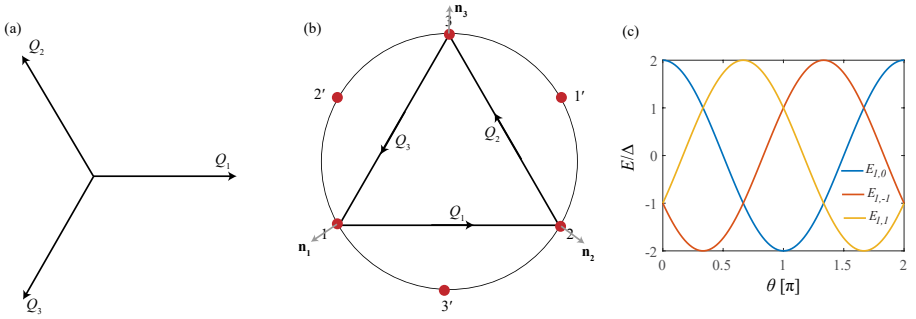
$$H'_{\rm CDW}(\boldsymbol{k}) = \begin{pmatrix} v_F\boldsymbol{k}\cdot\hat{\boldsymbol{n}}'_1 & \Delta e^{i\theta_1} & \Delta e^{-i\theta_3} \\ \Delta e^{-i\theta_1} & v_F\boldsymbol{k}\cdot\hat{\boldsymbol{n}}'_2 & \Delta e^{i\theta_2} \\ \Delta e^{i\theta_3} & \Delta e^{-i\theta_2} & v_F\boldsymbol{k}\cdot\hat{\boldsymbol{n}}'_3 \end{pmatrix}. \tag{S6}$$

Next, let us deduce the symmetry operations for the effective Hamiltonian. First of all, it is easy to show that the system respects the spinless time-reversal symmetry $\mathcal{T} = K$ (K the conjugate)

$$\mathcal{T} H'_{\rm CDW}(-\boldsymbol{k}) \mathcal{T}^{-1} = H_{\rm CDW}(\boldsymbol{k}). \tag{S7}$$

The representation of out-of-plane three-fold rotation can be written as

$$U_{C_3} = \begin{pmatrix} 0 & 1 & 0 \\ 0 & 0 & 1 \\ 1 & 0 & 0 \end{pmatrix}. \tag{S8}$$



Supplementary Figure 1. (a) Triple Q vectors: $\boldsymbol{Q}_1$, $\boldsymbol{Q}_2$, $\boldsymbol{Q}_3$. (b) Six hot spots in k-space, where the gap opening due to density waves overlap. These six hot spots can be classified into two groups:(1,2,3) and (1′,2′,3′). (c) The energy $E_{J,m}$ versus θ with $J = 1$, $m = 0, \pm 1$.

Then it is straightforward to show that under the C_3 operation,

$$U_{C_3} H_{\mathrm{CDW}}(C_3\boldsymbol{k}) U_{C_3}^{-1} = \begin{pmatrix} v_F \boldsymbol{k}\cdot\hat{\boldsymbol{n}}_1 & \Delta e^{-i\theta_2} & \Delta e^{i\theta_1} \\ \Delta e^{i\theta_2} & v_F \boldsymbol{k}\cdot\hat{\boldsymbol{n}}_2 & \Delta e^{-i\theta_3} \\ \Delta e^{-i\theta_1} & \Delta e^{i\theta_3} & v_F \boldsymbol{k}\cdot\hat{\boldsymbol{n}}_3 \end{pmatrix}. \tag{S9}$$

We can see that the system preserves C_3 symmetry $U_{C_3} H_{\mathrm{CDW}}(C_3\boldsymbol{k}) U_{C_3}^{-1} = H_{\mathrm{CDW}}(C_3\boldsymbol{k})$ if $\theta_1 = \theta_2 = \theta_3 = \theta$. Similarly, $U_{C_3} H'_{\mathrm{CDW}}(C_3\boldsymbol{k}) U_{C_3}^{-1} = H'_{\mathrm{CDW}}(C_3\boldsymbol{k})$ so that the full system respects C_3 symmetry. Hence, we would fix the $\theta_1 = \theta_2 = \theta_3$ in our discussion.

It can be found that when $\theta = \frac{n\pi}{3}$ (n are integers), the system further respects the inversion symmetry and M_x:

$$I H'_{\mathrm{CDW}}(-\boldsymbol{k}) I^{-1} = H_{\mathrm{CDW}}(\boldsymbol{k}), \tag{S10}$$

$$M_x H_{\mathrm{CDW}}(-k_x, k_y) M_x^{-1} = H_{\mathrm{CDW}}(k_x, k_y). \tag{S11}$$

Let us show the above two equations in more detail. The mirror M_x operation maps k_x to $-k_x$, and exchanges hot spots 1 and 2 within the same group. As a result,

$$\begin{aligned} M_x H_{\mathrm{CDW}}(-k_x, k_y) M_x^{-1} &= \begin{pmatrix} 0 & 1 & 0 \\ 1 & 0 & 0 \\ 0 & 0 & 1 \end{pmatrix} \begin{pmatrix} v_F(\frac{\sqrt{3}}{2}k_x - \frac{1}{2}k_y) & \Delta e^{-i\theta} & \Delta e^{i\theta} \\ \Delta e^{i\theta} & v_F(-\frac{\sqrt{3}}{2}k_x - \frac{1}{2}k_y) & \Delta e^{-i\theta} \\ \Delta e^{-i\theta} & \Delta e^{i\theta} & v_F k_y \end{pmatrix} \begin{pmatrix} 0 & 1 & 0 \\ 1 & 0 & 0 \\ 0 & 0 & 1 \end{pmatrix} \\ &= \begin{pmatrix} v_F \boldsymbol{k}\cdot\hat{\boldsymbol{n}}_1 & \Delta e^{i\theta} & \Delta e^{-i\theta} \\ \Delta e^{-i\theta} & v_F \boldsymbol{k}\cdot\hat{\boldsymbol{n}}_2 & \Delta e^{i\theta} \\ \Delta e^{i\theta} & \Delta e^{-i\theta} & v_F \boldsymbol{k}\cdot\hat{\boldsymbol{n}}_3 \end{pmatrix}. \end{aligned} \tag{S12}$$

When $\theta = -\theta$, i.e., $\theta = n\pi$, Eq. (S12) becomes $H_{\mathrm{CDW}}(\boldsymbol{k})$. It is also worth noting that when $\theta_1 + \theta_2 + \theta_3 = 3\theta = 2n\pi$, the ground states are the same [21]. In other words, the system exhibits a periodicity of $\frac{2\pi}{3}$. As a result, when $\theta = n\pi/3$, we generally expect $M_x H_{\mathrm{CDW}}(-k_x, k_y) M_x^{-1} = H_{\mathrm{CDW}}(k_x, k_y)$, i.e., the presence of mirror symmetry. Similarly, the relation Eq. (S10) can be shown. Note that the effects of inversion and out-of-plane C_2 are the same here, which maps momentum $\boldsymbol{k}$ to $-\boldsymbol{k}$, and maps one group hot spots to the other group.

Finally, for all θ, the system exhibits M_y symmetry:

$$M_y H_{\mathrm{CDW}}(k_x, -k_y) M_y^{-1} = H'_{\mathrm{CDW}}(k_x, k_y). \tag{S13}$$

In the main text, we have mapped $H_{\mathrm{CDW}}(\boldsymbol{k})$ as a three-band massive Dirac Hamiltonian. Now we present the details here. We can solve the eigenstates of $H(\boldsymbol{k})$ analytically at the hot spots ($\boldsymbol{k} = 0$):

$$\begin{aligned} E_{1,0} &= 2\Delta\cos\theta, \\ E_{1,-1} &= 2\Delta\cos(\frac{2\pi}{3} + \theta), \\ E_{1,1} &= 2\Delta\cos(\frac{4\pi}{3} + \theta). \end{aligned} \tag{S14}$$

See Supplementary Fig. 1 for a plot of these three energy levels versus θ. The corresponding eigenstates are

$$\begin{aligned}|E_{1,0}\rangle &= \frac{1}{\sqrt{3}}(|p_1\rangle + |p_2\rangle + |p_3\rangle),\\ |E_{1,-1}\rangle &= \frac{1}{\sqrt{3}}(e^{i\frac{\pi}{3}}|p_1\rangle + e^{-i\frac{\pi}{3}}|p_2\rangle + e^{i\pi}|p_3\rangle),\\ |E_{1,1}\rangle &= \frac{1}{\sqrt{3}}(e^{i\frac{2\pi}{3}}|p_1\rangle + e^{i\frac{4\pi}{3}}|p_2\rangle + |p_3\rangle).\end{aligned} \tag{S15}$$

where $|p_j\rangle$ labels the wavefunction of j-th hot spots, the eigenstates as $|E_{J,m}\rangle$ with J as the total angular momentum number, m as the magnetic quantum number. It is easy to verify that $C_3|E_{J,m}\rangle = e^{-i\frac{2m\pi}{3}}|E_{J,m}\rangle$ under the splinless C_3 operation. Then we can project the Hamiltonian in the basis spanned by $(|E_{1,0}\rangle, |E_{1,-1}\rangle, |E_{1,1}\rangle)$:

$$H^{\text{eff}}_{\text{CDW}}(\boldsymbol{k}) = \begin{pmatrix} E_{1,0} & -\frac{i}{2}v_F k_- & -\frac{i}{2}v_F k_+ \\ \frac{i}{2}v_F k_+ & E_{1,-1} & -\frac{i}{2}v_F k_- \\ \frac{i}{2}v_F k_- & \frac{i}{2}v_F k_+ & E_{1,1}\end{pmatrix} \tag{S16}$$

B. Effective Hamiltonian and symmetry analysis for the Triple-Q SDW state

As mentioned in the main text, we can express the SDW states with the superposition of spiral spin textures

$$\boldsymbol{S}_i^{spiral} = \Delta\sum_{\nu=1}^{3}(\sin\mathcal{Q}_\nu\cos\phi_\nu, \sin\mathcal{Q}_\nu\sin\phi_\nu, -\cos\mathcal{Q}_\nu). \tag{S17}$$

where i is the site index, $\phi_\nu = \frac{2}{3}\pi(\nu-1)$, $\mathcal{Q}_\nu = \boldsymbol{Q}_\nu\cdot\boldsymbol{r}_i + \theta_\nu$.

It is easy to verify that the spin Hamiltonian caused by the SDW states is C_3 invariant:

$$H_s = \sum_i \boldsymbol{S}_i^{spiral}\cdot\boldsymbol{\sigma}. \tag{S18}$$

Then, we can obtain the effective Hamiltonian near the first group hot spots (1,2, and 3) as

$$H_{\text{SDW}}(\boldsymbol{k}) = \begin{pmatrix} v_F\boldsymbol{k}\cdot\boldsymbol{n}_1 & \Delta\boldsymbol{S}_{-\boldsymbol{Q}_1}\cdot\boldsymbol{\sigma} & \Delta\boldsymbol{S}_{\boldsymbol{Q}_3}\cdot\boldsymbol{\sigma} \\ \Delta\boldsymbol{S}_{\boldsymbol{Q}_1}\cdot\boldsymbol{\sigma} & v_F\boldsymbol{k}\cdot\boldsymbol{n}_2 & \Delta\boldsymbol{S}_{-\boldsymbol{Q}_2}\cdot\boldsymbol{\sigma} \\ \Delta\boldsymbol{S}_{-\boldsymbol{Q}_3}\cdot\boldsymbol{\sigma} & \Delta\boldsymbol{S}_{\boldsymbol{Q}_2}\cdot\boldsymbol{\sigma} & v_F\boldsymbol{k}\cdot\boldsymbol{n}_3\end{pmatrix}. \tag{S19}$$

where the basis is $(c_{1\boldsymbol{k},\uparrow}, c_{1\boldsymbol{k},\downarrow}, c_{2\boldsymbol{k},\uparrow}, c_{2\boldsymbol{k},\downarrow}, c_{3\boldsymbol{k},\uparrow}, c_{3\boldsymbol{k},\downarrow})^T$, and

$$\boldsymbol{S}_{\boldsymbol{Q}_\nu} = (-\frac{i}{2}\cos\phi_\nu, -\frac{i}{2}\sin\phi_\nu, -\frac{1}{2})e^{i\theta_\nu}, \tag{S20}$$

$$\boldsymbol{S}_{-\boldsymbol{Q}_\nu} = (\frac{i}{2}\cos\phi_\nu, \frac{i}{2}\sin\phi_\nu, -\frac{1}{2})e^{-i\theta_\nu}. \tag{S21}$$

Near the second group hot spots ($1'$, $2'$, and $3'$), the effective Hamiltonian is

$$H'_{\text{SDW}}(\boldsymbol{k}) = \begin{pmatrix} v_F\boldsymbol{k}\cdot\boldsymbol{n}'_1 & \Delta\boldsymbol{S}_{\boldsymbol{Q}_1}\cdot\boldsymbol{\sigma} & \Delta\boldsymbol{S}_{-\boldsymbol{Q}_3}\cdot\boldsymbol{\sigma} \\ \Delta\boldsymbol{S}_{-\boldsymbol{Q}_1}\cdot\boldsymbol{\sigma} & v_F\boldsymbol{k}\cdot\boldsymbol{n}'_2 & \Delta\boldsymbol{S}_{\boldsymbol{Q}_2}\cdot\boldsymbol{\sigma} \\ \Delta\boldsymbol{S}_{\boldsymbol{Q}_3}\cdot\boldsymbol{\sigma} & \Delta\boldsymbol{S}_{-\boldsymbol{Q}_2}\cdot\boldsymbol{\sigma} & v_F\boldsymbol{k}\cdot\boldsymbol{n}'_3\end{pmatrix} \tag{S22}$$

Again, we can easily show that the system respects the out-of-plane C_{3z} symmetry if $\theta = \theta_1 = \theta_2 = \theta_3$ with

$$\begin{aligned}U_{C_{3z}}H_{\text{SDW}}(C_3\boldsymbol{k})U^{-1}_{C_{3z}} &= H_{\text{SDW}}(\boldsymbol{k}),\\ U_{C_{3z}}H'_{\text{SDW}}(C_3\boldsymbol{k})U^{-1}_{C_{3z}} &= H'_{\text{SDW}}(\boldsymbol{k}),\end{aligned} \tag{S23}$$

where the representation of C_3 operation is

$$U_{C_3} = \begin{pmatrix}0&1&0\\0&0&1\\1&0&0\end{pmatrix}\otimes e^{-i\frac{\pi}{3}\sigma_z}. \tag{S24}$$

It can also be seen that the system breaks the time-reversal symmetry $\hat{T} = i\sigma_y K$, with

$$\hat{T} H'_{\mathrm{SDW}}(-\boldsymbol{k})\hat{T}^{-1} \neq H_{\mathrm{SDW}}(\boldsymbol{k}). \tag{S25}$$

The inversion symmetry is also broken in general:

$$\hat{I} H'_{\mathrm{SDW}}(-\boldsymbol{k})\hat{I}^{-1} \neq H_{\mathrm{SDW}}(\boldsymbol{k}). \tag{S26}$$

But there is an emergent 'particle-hole' symmetry:

$$H_{\mathrm{SDW}}(\boldsymbol{k}) = -\hat{T} H'_{SDW}(\boldsymbol{k})\hat{T}^{-1}, \tag{S27}$$

and it further respects the combined symmetry $\hat{M}_y\hat{T}$ for arbitrary θ with

$$U_{\hat{M}_y\hat{T}} = \begin{pmatrix} 0 & -i\sigma_y & 0 \\ -i\sigma_y & 0 & 0 \\ 0 & 0 & -i\sigma_y \end{pmatrix} i\sigma_y K = \begin{pmatrix} 0 & \sigma_0 & 0 \\ \sigma_0 & 0 & 0 \\ 0 & 0 & \sigma_0 \end{pmatrix} K \tag{S28}$$

and

$$U_{\hat{M}_y\hat{T}} H_{\mathrm{SDW}}(-k_x, k_y) U^{-1}_{\hat{M}_y\hat{T}} = H_{\mathrm{SDW}}(k_x, k_y). \tag{S29}$$

It can also be shown that the system would respect C_{2z} symmetry at $\theta = \frac{n\pi}{3}$:

$$C_{2z} H_{\mathrm{SDW}}(\boldsymbol{k}, \theta = \frac{n\pi}{3}) C_{2z}^{-1} = H'_{\mathrm{SDW}}(-\boldsymbol{k}, \theta = \frac{n\pi}{3}). \tag{S30}$$

In other words, the point group of this triple-Q SDW is C_6 at $\theta = \frac{n\pi}{3}$ and reduces to C_3 at other angles.

Being similar to the CDW analysis, we can perform a unitary transform and rewrite the Hamiltonian in the basis $(|E_{1,0}\rangle \otimes |\uparrow\rangle, |E_{1,1}\rangle \otimes |\downarrow\rangle, |E_{1,-1}\rangle \otimes |\uparrow\rangle, |E_{1,0}\rangle \otimes |\downarrow\rangle, |E_{1,1}\rangle \otimes |\uparrow\rangle, |E_{1,-1}\rangle \otimes |\downarrow\rangle)^T$, which carries the eigenvalues of $(e^{-i\frac{\pi}{3}}, e^{-i\frac{\pi}{3}}, e^{i\frac{\pi}{3}}, e^{i\frac{\pi}{3}}, 1, 1)$ under C_3 operation. Then we obtain the effective Hamiltonian

$$H^{\mathrm{eff}}_{\mathrm{SDW}}(\boldsymbol{k}) = \begin{pmatrix} H_{11} & -\frac{i}{2}k_-\sigma_z & -\frac{i}{2}k_-\sigma_z \\ \frac{i}{2}k_+\sigma_z & H_{22} & -\frac{i}{2}k_-\sigma_0 \\ \frac{i}{2}k_+\sigma_z & \frac{i}{2}k_+\sigma_0 & H_{33} \end{pmatrix}, \tag{S31}$$

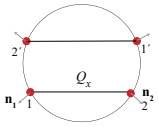
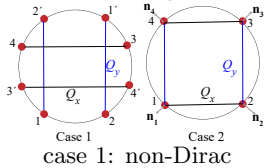
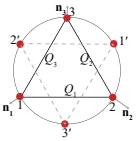
where the terms

$$\begin{aligned} H_{11}(\theta) &= -\frac{\sqrt{3}}{2}\Delta\cos(\theta + \frac{\pi}{6})\sigma_0 + \Delta\cos(\theta + \frac{\pi}{6})\sigma_x \\ &\quad - \frac{\Delta}{2}\sin(\theta + \frac{\pi}{6})\sigma_z, \\ H_{22}(\theta) &= \frac{\sqrt{3}}{2}\Delta\cos(\theta - \frac{\pi}{6})\sigma_0 + \Delta\cos(\theta - \frac{\pi}{6})\sigma_x \\ &\quad + \frac{\Delta}{2}\sin(\theta - \frac{\pi}{6})\sigma_z, \\ H_{33}(\theta) &= -\frac{\sqrt{3}}{2}\Delta\sin\theta\sigma_0 - \Delta\sin\theta\sigma_x + \frac{\Delta}{2}\cos\theta\sigma_z. \end{aligned} \tag{S32}$$

Supplementary Note 2. SINGLE-Q AND DOUBLE-Q STATES

After identifying the low-energy Dirac Hamiltonians induced by the triple-Q order parameters, one natural question is whether such low-energy Dirac Hamiltnmoians can appear in other density waves systems with different numbers of Q-vectors, such as single Q and double-Q vectors. As an exploration, we consider the single-Q CDW order parameter $\Delta(\boldsymbol{r}) = 2\Delta\cos(Q_x x)$ and double-Q CDW order parameter $\Delta(\boldsymbol{r}) = 2\Delta\sum_{\nu=x,y}\cos(\boldsymbol{Q}_\nu \cdot \boldsymbol{r})$. It is worth noting that, unlike the triple-Q density waves, the single-Q and double-Q density waves do not have internal degrees of freedom. While phasons can be excited in the moving density waves, the phase shift θ is absent in the static single-Q and double-Q density waves. The hot spots connected by the single-Q and double-Q vectors on the Fermi circle are highlighted in Supplementary Table 1. Following the previous section, we can perform a parallel analysis of the

Supplementary Table 1. The comparison between density waves with different numbers of Q-vectors.

CDW	single-Q	double-Q	triple-Q
Oder parameter	$\Delta(\boldsymbol{r}) = 2\Delta\cos(Q_x x)$	$\Delta(\boldsymbol{r}) = 2\Delta\sum_{\nu=x,y}\cos(\boldsymbol{Q_\nu}\cdot\boldsymbol{r})$	$\Delta(\boldsymbol{r}) = 2\Delta\sum_{\nu=1}^{3}\cos(\boldsymbol{Q_\nu}\cdot\boldsymbol{r}+\theta)$
hot spots		 Case 1 Case 2	
low-energy Hamiltonian	non-Dirac	case 1: non-Dirac case 2: multi-band Dirac	multi-band Dirac

low-energy effective Hamiltonian of single/double-Q case. In the single-Q case, the effective Hamiltonian defined in the band basis at $\boldsymbol{k} = 0$ is

$$\mathcal{H}^{1Q}_{\text{eff}}(\boldsymbol{k}) = \begin{pmatrix} -\Delta - k_y\sin\alpha & k_x\cos\alpha \\ k_x\cos\alpha & \Delta - k_y\sin\alpha \end{pmatrix} \tag{S33}$$

Here, the angle α labels the unit vector direction along the hot spot momenta. Evidently, it is non-Dirac.

In the double-Q case, there would be four hot spots on the Fermi circles connected by either Q_x or Q_y vectors (see Supplementary Table 1). We shall separate it into two cases: (i) the hot spots on the Fermi surface connected by Q_x and Q_y are different; (ii) the hot spots on the Fermi surface connected by Q_x and Q_y are the same. Note that case 1 can be continuously tuned into case 2 by changing the parameters, such as the chemical potential. In the former case, every two hot spots give a 1D effective Hamiltonian as $\mathcal{H}^{1Q}_{\text{eff}}(\boldsymbol{k})$ so that the Dirac features are absent. In the second case, all four hot spots are connected by Q-vectors (see Supplementary Table 1) and the effective Hamiltonian can display multi-band Dirac behaviors.

We now look at the second case in more detail. To be specific, we set $Q_x = (1,0)Q, Q_y = (0,1)Q$. In the double-Q case (the case 2 in Table 1),

$$H^{2Q}_{\text{CDW}}(\boldsymbol{k}) = \begin{pmatrix} v_F\boldsymbol{k}\cdot\hat{n}_1 & \Delta & 0 & \Delta \\ \Delta & v_F\boldsymbol{k}\cdot\hat{\boldsymbol{n}}_2 & \Delta & 0 \\ 0 & \Delta & v_F\boldsymbol{k}\cdot\hat{\boldsymbol{n}}_3 & \Delta \\ \Delta & 0 & \Delta & v_F\boldsymbol{k}\cdot\hat{\boldsymbol{n}}_4 \end{pmatrix}. \tag{S34}$$

Here, the unit vectors $\hat{\boldsymbol{n}}_1 = \frac{1}{\sqrt{2}}(-1,-1), \hat{\boldsymbol{n}}_2 = \frac{1}{\sqrt{2}}(1,-1), \hat{\boldsymbol{n}}_3 = \frac{1}{\sqrt{2}}(1,1), \hat{\boldsymbol{n}}_4 = \frac{1}{\sqrt{2}}(-1,1)$. At $\boldsymbol{k} = 0$, the eigenenergies are $E_1 = 2\Delta$, $E_2 = 0$, $E_3 = -2\Delta$, $E_4 = 0$. The corresponding eigenstates are

$$\begin{aligned} |E_1\rangle &= \frac{1}{2}(|p_1\rangle + |p_2\rangle + |p_3\rangle + |p_4\rangle), \\ |E_2\rangle &= \frac{1}{2}(i\,|p_1\rangle - |p_2\rangle - i\,|p_3\rangle + |p_4\rangle), \\ |E_3\rangle &= \frac{1}{2}(-\,|p_1\rangle + |p_2\rangle - |p_3\rangle + |p_4\rangle), \\ |E_4\rangle &= \frac{1}{2}(-i\,|p_1\rangle - |p_2\rangle + i\,|p_3\rangle + |p_4\rangle). \end{aligned} \tag{S35}$$

Projecting $H^{2Q}_{\text{CDW}}(\boldsymbol{k})$ into the basis spanned by $(|E_1\rangle, |E_2\rangle, |E_3\rangle, |E_4\rangle)$, we obtain a four-band Dirac Hamiltonian:

$$\mathcal{H}^{2Q}_{\text{eff}}(\boldsymbol{k}) = \begin{pmatrix} 2\Delta & \tilde{v}_F k_+ & 0 & \tilde{v}_F^* k_- \\ \tilde{v}_F^* k_- & 0 & \tilde{v}_F k_+ & 0 \\ 0 & \tilde{v}_F^* k_- & -2\Delta & \tilde{v}_F k_+ \\ \tilde{v}_F k_+ & 0 & \tilde{v}_F^* k_- & 0 \end{pmatrix}. \tag{S36}$$

Here, $\tilde{v}_F = \frac{v_F}{2}e^{-i\frac{3\pi}{4}}$. In other words, the double-Q density waves can also induce the multi-band Dirac Hamiltonian and exhibit nontrivial band geometry. Note that $\mathcal{H}^{2Q}_{\text{eff}}(\boldsymbol{k})$ is the total Hamiltnoian for the double-Q CDW already, and its dimension is smaller than $\mathcal{H}^{3Q}_{\text{CDW},t}(\boldsymbol{k})$. It can be seen that $\mathcal{H}^{2Q}_{\text{eff}}(\boldsymbol{k})$ is a four-band Dirac Hamiltonian and exhibit nontrivial band geometry.

The comparison of density waves with different numbers of Q-vectors is summarized in Supplementary Table 1. Our analysis shows that multiband Dirac Hamiltonians can be induced by multi-Q density wave order parameters as long as more than two hot spots are folded together simultaneously. This conclusion is expected to hold even when the CDW order parameter is replaced with SDW order parameters, although the effective dimension of the Hamiltonian would be doubled.

Supplementary Note 3. NONRECIPROCAL TRANSPORTS IN TRIPLE-Q SDWS

A. Magnetochiral anisotropy in triple-Q SDWs

We consider a time-dependent drive

$$\mathcal{E}(t) = \boldsymbol{E}\cos(\omega t). \tag{S37}$$

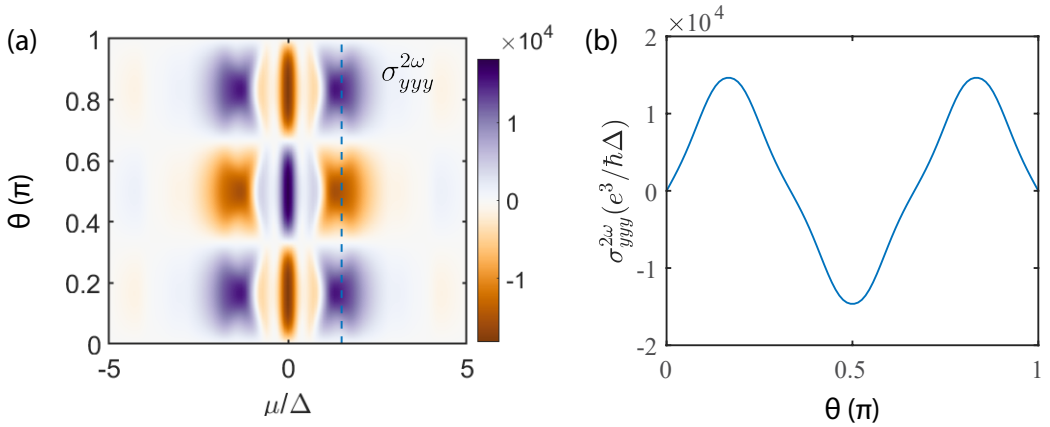
Without loss of generality, we set the electric field $\boldsymbol{E}$ along x-direction. In the experiment, it is convenient to identify the magnetochiral anisotropy by measuring the second harmonic generation of longitudinal conductivity [42]. Following the previous works [43, 44], it can be deduced that the nonreciprocal longitudinal charge transport can be given by

$$\sigma^{2\omega}_{\alpha\alpha\alpha} = -\frac{e^3}{2\hbar^3(2i\omega+\tau^{-1})(i\omega+\tau^{-1})}\int\frac{d\boldsymbol{k}}{(2\pi)^d}\sum_n f_n^{(0)}\frac{\partial^3\epsilon_n^{(0)}}{\partial k_\alpha^3} - \frac{2e^3}{\hbar}\int\frac{d\boldsymbol{k}}{(2\pi)^d}f_n^{(0)}\partial_{k_\alpha}G_n^{\alpha\alpha}(2\omega) \tag{S38}$$

where $f_n^{(0)}$ is the Fermi distribution for the n-th band $\epsilon_n^{(0)}$, and the band-renormalized quantum metric is defined as

$$G_n^{ab}(2\omega) = -\frac{1}{4}\sum_{l\neq n}\left(\frac{\mathcal{A}_{nl}^a\mathcal{A}_{ln}^b}{-\hbar\omega+\epsilon_{ln}} + \frac{\mathcal{A}_{nl}^b\mathcal{A}_{ln}^a}{\hbar\omega+\epsilon_{ln}}\right). \tag{S39}$$

Here, $A^a_{mn} = \frac{\langle n\boldsymbol{k}|\partial_a H|m\boldsymbol{k}\rangle}{\epsilon_{nm}}$ denotes the Berry connection between $n-$th and $l-$th band with $\epsilon_{nm} = \epsilon_n^{(0)} - \epsilon_m^{(0)}$. In the DC transport limit, we are interested in $\omega \to 0$. In this case, the additional antiunitary symmetry $\hat{M}_y\hat{T}$ in triple-Q SDW would enforce $\sigma^{2\omega}_{xxx} = 0$ by mapping k_x to -k_x. Instead, we would focus on $\sigma^{2\omega}_{yyy}$ below. The results are summarized in Supplementary Fig. 2. It can be seen from (a) and (b) that $\sigma^{2\omega}_{yyy}$ is generally finite expect for at $\theta = \frac{n\pi}{3}$ due to the presence of C_{2z} symmetry. Note that we also find that the quantum metric contribution in Eq. S38 is negligible.



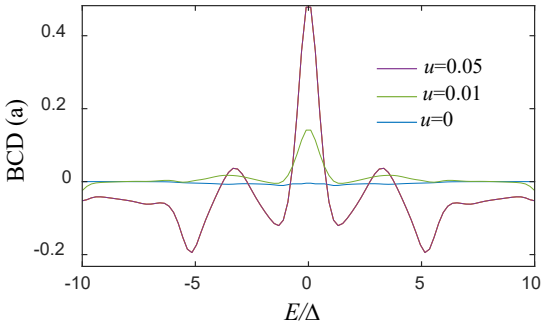
Supplementary Figure 2. The magnetochiral anisotropy represented by the strength of $\sigma^{2\omega}_{yyy}$ (in units of $\frac{e^3}{\hbar\Delta}$).(a) the phase shift dependence and chemical potential dependence of $\sigma^{2\omega}_{yyy}$ calculated from the SDW effective Hamiltonian. (b) A line-cut of (a) at a fixed $\mu = 1.5\Delta$. Here, the used parameters are $v_F = 100$, $\Delta = 1$, $T = 0.01\Delta$, $\tau = 0.01\Delta/\hbar$.

B. Possible nonlinear Hall effects in strained triple-Q SDWs

In the main text, we mostly focus on the C_3 invariant case. However, the C_3 symmetry can be broken externally. The question is whether any interesting effects are allowed in this case. In this Supplementary Information section,

Supplementary Table 2. Symmetry classification of momentum, spin, and strain tensor according to the irreducible representations of C_3 point group.

Irrep	Time-reversal Even	Time-reversal odd
A_1	$u_{xx}+u_{yy}$	σ_z
E	$(u_{xx}-u_{yy}, -2u_{xy})$	(k_x,k_y), (σ_x,σ_y)



[h]

Supplementary Figure 3. Nonlinear Hall effects in strained SDW crystals. The Berry curvature dipole (BCD) versus the energy E, where E is artificially tuned from $[-10,10]\Delta$ and $E=0$ is the Fermi energy. The strain strength is characterized by $u=0.05, 0.01, 0$, respectively. It can be seen that the BCD vanishes without strain due to the presence of C_3 symmetry, while there appears a sizable Berry curvature dipole when the SDW crystal is strained. Here, the used parameters in the triple-Q SDW effective Hamiltonian are $\Delta=1$, $v_F=100\Delta$, $\theta=0$, $\mu=0$.

we demonstrate that the nonlinear Hall effects are possible in strained triple-Q SDWs, such as strained SkX.

To the leading order terms, as shown in Table SI, the time-reversal invariant strain Hamiltonian is

$$H_{strain}=v_F\sum_{\alpha\alpha}u_\alpha\Gamma_0\otimes\sigma_0+v_F[(u_{xx}-u_{yy})k_x-2u_{xy}k_y]\Gamma_0\otimes\sigma_z, \tag{S40}$$

where Γ_0 is a three-by-three identify matrix in the hot spots space, the other group takes the same form. The first term is to effectively shift the chemical potential so we can neglect it. The strain Hamiltonian is simplified as

$$H_{strain}\approx v_F[(u_{xx}-u_{yy})k_x-2u_{xy}k_y]\Gamma_0\otimes\sigma_z. \tag{S41}$$

Without loss of generality, we can consider the uniaxial strain tensor to be

$$\begin{pmatrix}u_{xx} & u_{xy}\\ u_{yx} & u_{yy}\end{pmatrix}=u'\begin{pmatrix}\cos^2\varphi-\nu\sin^2\varphi & (1+\nu)\cos\varphi\sin\varphi\\ (1+\nu)\cos\varphi\sin\varphi & -\nu\cos^2\varphi+\sin^2\varphi\end{pmatrix} \tag{S42}$$

where φ is to label the strain direction, ν is the Poisson ratio.

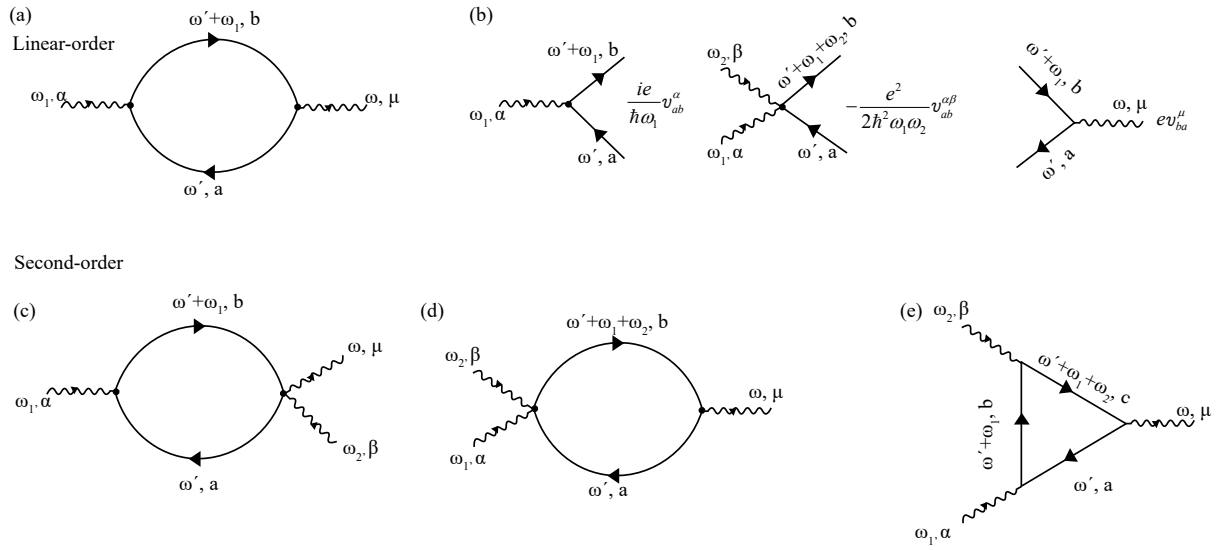
For simplicity, we set $\varphi=\pi/4$, and $u=(1+\nu)u'$, the strain Hamiltonian becomes

$$H_{strain}\approx -v_F u k_y\Gamma_0\otimes\sigma_z, \tag{S43}$$

where u characterizes the strain strength. Note that $u\neq 0$, the three-fold symmetry is broken. Then we can add the strain Hamiltonian into the total triple-Q Hamiltonian (note that we need to consider two sets of hot spots). The Berry curvature dipole is given by [30]

$$D_{\beta\gamma}=-\sum_n\int\frac{d\boldsymbol{k}}{(2\pi)^d}\frac{\partial\epsilon_{n\boldsymbol{k}}}{\partial\boldsymbol{k}_\beta}\Omega_{n\gamma}(\boldsymbol{k})\frac{\partial f(\epsilon_{n\boldsymbol{k}})}{\partial\epsilon_{n\boldsymbol{k}}}. \tag{S44}$$

The calculated strained induced finite Berry curvature dipole D_{yz} is shown in Supplementary Fig. 3. It can be seen that there can support finite Berry curvature dipole in strained triple-Q SDW systems.



Supplementary Figure 4. (a) The bubble diagram for the linear optical responses. (b) The vortex diagrams. (c) to (e) The Feynman diagrams for the second-order nonlinear optical response.

Supplementary Note 4. SECOND HARMONIC GENERATION RESPONSES FORMALISM

We reproduce the optical responses formula given by ref. [37, 38] here, which has been used in the main text to calculate the SHG below. The linear optical conductivity is given by the bubble diagram [Supplementary Fig. 3(a)],

$$\begin{aligned}\sigma^{\mu\alpha}(\omega;\omega) &= \frac{ie^2}{\hbar\omega_1}\sum_{a\neq b}\int[d\boldsymbol{k}]\int d\omega' G_a(\omega')v^{\alpha}_{ab}G_b(\omega'+\omega_1)v^{\mu}_{ba}\\ &= \frac{ie^2}{\hbar\omega}\sum_{a\neq b}\int[d\boldsymbol{k}]\frac{f_{ab}v^{\alpha}_{ab}v^{\mu}_{ba}}{\omega-\epsilon_{ba}}.\end{aligned} \tag{S45}$$

where $[d\boldsymbol{k}]=\int\frac{d\boldsymbol{k}}{(2\pi)^d}$, $v^{\alpha}_{ab}=\langle a|\partial_{k_\alpha}H(\boldsymbol{k})|b\rangle$, $H(\boldsymbol{k})$ is the Hamiltonian, the Fermi Dirac function difference between two bands $f_{ab}=f_a-f_b$, $\epsilon_{ba}=\epsilon_b-\epsilon_a$.

As shown in Supplementary Fig. 3, the second-order nonlinear optical conductivity is given by

$$\begin{aligned}\sigma^{\mu\alpha\beta}(\omega_1+\omega_2;\omega_1,\omega_2) &= -\frac{e^3}{2\hbar^2\omega_1\omega_2}\sum_{a,b,c}\int[d\boldsymbol{k}]\int d\omega'[G_a(\omega')v^{\alpha}_{ab}G_b(\omega'+\omega_1)v^{\mu\beta}_{ba}+\frac{1}{2}G_a(\omega')v^{\alpha\beta}_{ab}G_b(\omega'+\omega_1+\omega_2)v^{\mu}_{ba}+\\ &G_a(\omega')v^{\alpha}_{ab}G_b(\omega'+\omega_1)v^{\beta}_{bc}G_c(\omega'+\omega_1+\omega_2)v^{\mu}_{ca}]+(\omega_1,\alpha)\leftrightarrow(\omega_2,\beta),\\ &= -\frac{e^3}{2\hbar^2\omega_1\omega_2}\int[d\boldsymbol{k}][f_{ab}(\frac{v^{\alpha}_{ab}v^{\mu\beta}_{ba}}{\omega_1-\epsilon_{ba}}+\frac{v^{\beta}_{ab}v^{\mu\alpha}_{ba}}{\omega_2-\epsilon_{ba}})+f_{ab}\frac{v^{\alpha\beta}_{ab}v^{\mu}_{ba}}{\omega_1+\omega_2-\epsilon_{ab}}\\ &+v^{\alpha}_{ab}v^{\beta}_{bc}v^{\mu}_{ca}(\frac{f_{ab}}{(\omega_1-\epsilon_{ba})(\omega_1+\omega_2-\epsilon_{ca})}+\frac{f_{cb}}{(\omega_2-\epsilon_{cb})(\omega_1+\omega_2-\epsilon_{ca})})\\ &+v^{\beta}_{ab}v^{\alpha}_{bc}v^{\mu}_{ca}(\frac{f_{ab}}{(\omega_2-\epsilon_{ba})(\omega_1+\omega_2-\epsilon_{ca})}+\frac{f_{cb}}{(\omega_1-\epsilon_{cb})(\omega_1+\omega_2-\epsilon_{ca})})].\end{aligned} \tag{S46}$$

Here, $v^{\alpha\beta}_{ab}=\langle a|\partial_{k_\alpha}\partial_{k_\beta}H(\boldsymbol{k})|b\rangle$. For the second-harmonic generation ($\omega_1=\omega_2=\omega$),

$$\begin{aligned}\sigma^{\mu\alpha\beta}(2\omega;\omega,\omega) = -\frac{e^3}{2\hbar^2\omega^2}\sum_{a,b,c}\int[d\boldsymbol{k}][f_{ab}\frac{v^{\alpha}_{ab}v^{\mu\beta}_{ba}+v^{\beta}_{ab}v^{\mu\alpha}_{ba}}{\omega-\epsilon_{ba}}+f_{ab}\frac{v^{\alpha\beta}_{ab}v^{\mu}_{ba}}{2\omega-\epsilon_{ab}}\\ +(v^{\alpha}_{ab}v^{\beta}_{bc}+v^{\beta}_{ab}v^{\alpha}_{bc})v^{\mu}_{ca}(\frac{f_{ab}}{(\omega-\epsilon_{ba})(2\omega-\epsilon_{ca})}+\frac{f_{cb}}{(\omega-\epsilon_{cb})(2\omega-\epsilon_{ca})})]\end{aligned} \tag{S47}$$

Using the identity:

$$\frac{f_{ab}}{(\omega-\epsilon_{ba})(2\omega-\epsilon_{ca})}+\frac{f_{cb}}{(\omega-\epsilon_{cb})(2\omega-\epsilon_{ca})}=\frac{1}{\epsilon_{ab}+\epsilon_{cb}}[\frac{2f_{ac}}{2\omega-\epsilon_{ca}}+\frac{f_{cb}}{\omega-\epsilon_{cb}}+\frac{f_{ba}}{\omega-\epsilon_{ba}}]. \tag{S48}$$

The optical conductivity for the second-harmonic generation can be rewritten as

$$\sigma^{\mu\alpha\beta} = \sigma_{\mathrm{I}}^{\mu\alpha\beta}+\sigma_{\mathrm{II}}^{\mu\alpha\beta}, \tag{S49}$$

$$\sigma_{\mathrm{I}}^{\mu\alpha\beta} = -\frac{e^3}{2\hbar^2\omega^2}\sum_{a\neq b}\int[d\boldsymbol{k}]f_{ab}\frac{v_{ab}^{\alpha}v_{ba}^{\mu\beta}+v_{ab}^{\beta}v_{ba}^{\mu\alpha}}{\omega-\epsilon_{ba}}+f_{ab}\frac{v_{ab}^{\alpha\beta}v_{ba}^{\mu}}{2\omega-\epsilon_{ab}}, \tag{S50}$$

$$\sigma_{\mathrm{II}}^{\mu\alpha\beta} = -\frac{e^3}{2\hbar^2\omega^2}\sum_{a\neq b\neq c}\int[d\boldsymbol{k}]\frac{(v_{ab}^{\alpha}v_{bc}^{\beta}+v_{ab}^{\beta}v_{bc}^{\alpha})v_{ca}^{\mu}}{\epsilon_{ab}+\epsilon_{cb}}(\frac{2f_{ac}}{2\omega-\epsilon_{ca}}+\frac{f_{cb}}{\omega-\epsilon_{cb}}+\frac{f_{ba}}{\omega-\epsilon_{ba}}), \tag{S51}$$

where 2ω and ω characterize the contributions from two-photon and one-photon processes, respectively. The contribution that involves two (three) different bands is labeled as $\sigma_{\mathrm{I}}^{\mu\alpha\beta}$ ($\sigma_{\mathrm{II}}^{\mu\alpha\beta}$), respectively.